

Preparation and Characterization of Ti/rGO-RuO₂ Electrode for Hydrogen and Oxygen Evolution Reactions

Xiaoyang Bao, Jiqing Bao*, Jie Xu, Cong Xu

School of Biological and Chemical Engineering, Jiaxing University, Jiaxing 314001, China;

*E-mail: 469784902@qq.com

Received: 11 May 2018 / Accepted: 15 June 2018 / Published: 5 July 2018

This paper presents a preparation method of a graphene RuO₂ composite electrode. The electrode is obtained via electrochemical reduction of graphene oxide (GO) on a Ti substrate followed by thermal decomposition to prepare RuO₂. According to results from SEM, CA curves, and EIS impedance, Ti/rGO-RuO₂ has many exposed active sites and good electrical conductivity. Ti/rGO-RuO₂ also shows excellent electrocatalytic performance for electrochemical water splitting (hydrogen evolution potential is -1.226 V and oxygen evolution potential is 0.842 V). After 10 h of electrolysis at 250 mA·cm⁻², the activity of Ti/rGO-RuO₂ showed no significant decrease for the hydrogen evolution reaction. In sum, Ti/rGO-RuO₂ contains an intermediate layer of graphene, has excellent application prospects in electrochemical water splitting, and has good application value in the field of hydroelectricity.

Keywords: metal oxide anode; graphene; water splitting

1. INTRODUCTION

Hydrogen has received increasing attention as a kind of clean and efficient energy. Electrochemical water splitting is considered to be an effective method for sustainably obtaining hydrogen. However, the energy consumption of electrolyzed water is large because of the presence of an overpotential. Catalysts are key to electrochemical water splitting technologies[1, 2] and have a direct impact on electrochemical reaction rates and overpotential. Thus, it is necessary to study electrode materials that have lower hydrogen overpotential. Pt is commonly used as a catalyst for the hydrogen evolution reaction (HER), and IrO₂ is used to accelerate the rate of the oxygen evolution reaction (OER). Pt has high catalytic activity and low HER overpotential and is a desirable material for electrochemical water splitting, but it is limited by its high cost. IrO₂ has poor reversibility, high

overpotential, and large energy loss in water electrolysis[3]. Therefore, Pt and IrO₂ cannot be widely used in water splitting. RuO₂ is a platinum-based metal oxide[4, 5] that has high catalytic activity. Calculation results of RuO₂ from X-ray photoelectron spectroscopy combined with density functional theory (DFT) calculations show that the unsaturated Ru (CUS Ru) in RuO₂ can reduce the energy barrier in electrochemical reactions[6-8]. Rutile RuO₂ accelerates the rate of OER and also has higher catalytic activity for HER during water splitting[9, 10]. Furthermore, RuO₂ can be coated on a Ti substrate via thermal decomposition to prepare an electrode that has high activity and is low cost. However, one of the major challenges of using RuO₂ as an anode for water splitting is the bad stability; RuO₂ is oxidized to RuO₄ and then dissolves, leading to the deactivation of RuO₂. This is particularly a problem on a dimensionally stable anode (DSA). Thus, enhancing the stability of RuO₂ is the goal of this study.

The electrocatalytic activity of an electrode generally depends on many factors, such as accessibility to the active center, conductivity, and electrode geometry. Nanostructured materials are the most direct way to improve electrocatalytic activity. To increase an electrochemical reaction rate, researchers generally use conductive materials as a carrier to increase the active sites and conductivity of a catalyst. Carbon nanomaterials that have excellent conductivity and specific surface area are research hotspots for catalyst carriers, such as carbon nanotubes[11], carbon nanofibers[12], nanocarbon[13], and graphene[14]. Graphene is a two-dimensional material with a large specific surface area (2630 m²·g⁻¹)[15] that can provide a large number of catalytically active sites[16-18], can be used for electrochemical reaction and excellent conductivity, can reduce contact resistance, and can enhance electronic transmission capacity in batteries[19-21], photoelectrics[22], sensors[23], and catalysts[24] in a wide range of applications. In addition, the excellent barrier properties[25] and chemical inertness[26] of graphene allow it to be used in corrosion-resistant materials. Graphene can be stacked to form a dense layer, which has a physical preservative effect on slowing or preventing corrosion through the medium. Chen[27] deposited a graphene layer on Cu using chemical vapor deposition (CVD), and the graphene-coated copper sheet exhibited extremely high oxidation resistance. Therefore, graphene is also excellent in the field of corrosion protection.

In summary, the characteristics of graphene include anti-infiltration, anti-oxidation, high specific surface area, and high conductance; thus, graphene can be used as a protective layer and a conductive layer to improve electron transfer between the Ti substrate and RuO₂ to obtain high catalytic activity and low overpotential for the hydrogen evolution anode Ti/rGO-RuO₂, which exhibits superior activity and stability for OER and HER.

2. EXPERIMENTAL

2.1. Materials

RuCl₃·xH₂O (Ru 37 wt%) and natural graphite powder were obtained from Sinopharm Chemical Reagent Co., Ltd. n-Butanol was used as a solvent to prepare all of the metal salt solutions.

2.2 Electrode preparation

The Ti substrate (TA2, 10 mm×10 mm×2 mm) was polished and etched with 10% oxalic acid for 2 h at 80°C to remove TiO₂. The treated Ti substrate was then washed with deionized water and stored in absolute ethanol. RuCl₃·xH₂O was dissolved in n-butanol to prepare a Ru metal salt solution (Ru³⁺ 0.04 mol·L⁻¹).

Natural graphite powder was peeled off via chemical oxidation to obtain graphite oxide (GO); for the specific experimental conditions, readers are referred to the work of Wu[20]. The prepared GO was mixed with secondary water and treated with an ultrasonic wave for 30 min to prepare a GO suspension (GO 0.85 mg·ml⁻¹). The treated Ti substrate was coated with a GO layer via dip-coating 20 μL of GO suspension on the Ti substrate and then drying at room temperature. The Ti substrate with the GO layer was used as a cathode and was reduced in phosphate buffer solution (0.5 mol·L⁻¹, pH 5.01) at -1.0V (vs. SCE) to prepare the Ti substrate with an rGO layer (Ti/rGO).

Ti/rGO was coated with 20 μL of Ru metal salt solution using the dip-coating method. After that, Ti/rGO was dried at 120°C for 10 min in a vacuum drying oven, and to decompose it, it was sintered at 450°C for 15 min in a muffle furnace. These steps for drying and sintering the Ru metal salt solution and the graphene suspension on the Ti substrate were repeated five times. Finally, the Ti substrates were sintered for 2 h at 450°C. The electrode prepared via the above steps is denoted as Ti/rGO-RuO₂. The Ti/RuO₂ electrode was prepared using a similar method but without the rGO layer.

2.3 Electrode characterization

Morphology, microstructure, and composition of the samples were investigated using SEM and XRD. SEM was carried out on a Hitachi S-4800 model instrument. XRD patterns were obtained with an X-ray diffractometer (DX-2600, Dandong Fangyuan Instrument Co., Ltd.) using Cu Kα radiation (1.54184 Å, 40 kV, 30 mA).

To test the performance of the Ti/rGO-RuO₂ electrode, linear sweep voltammetry (LSV), chronoamperometry (CA), and electrochemical impedance (EIS) measurements were conducted. All of the tests were carried out on an electrochemical workstation (CHI 660E, CH Instruments, Inc.) and were performed using a conventional three-electrode system. The Ti/rGO-RuO₂ electrode, a platinum-wire, and a saturated calomel electrode (SCE) were used as the working electrode, counter electrode, and reference electrode, respectively. All of the experiments were carried out at 25°C in 0.1 mol·L⁻¹ NaOH. The performances of hydrogen and oxygen evolution were tested using LSV at a scan rate of 100 mV·s⁻¹ over the ranges of 0~-2.0 V and 0~1.5 V, respectively. CA curves for Ti/RuO₂ and Ti/rGO-RuO₂ were recorded at open circuit potential with a potential step amplitude of 5 mV and a pulse width of 2 s. EIS were recorded at open circuit potential over a frequency range of 0.1 Hz to 10 kHz with an alternating signal of 5 mV. The stability of the Ti/rGO-RuO₂ electrode for HER and OER was evaluated using an accelerated service lifetime experiment at a current density of 250 mA·cm⁻². The service lifetime of the Ti/rGO-RuO₂ electrode is defined as the operation time when the potential of the cell increased rapidly to 5 V from the initial value. The change in cell voltage was recorded with respect to time to test the overall water splitting.

3. RESULTS AND DISCUSSION

3.1. Surface morphology and crystal structure

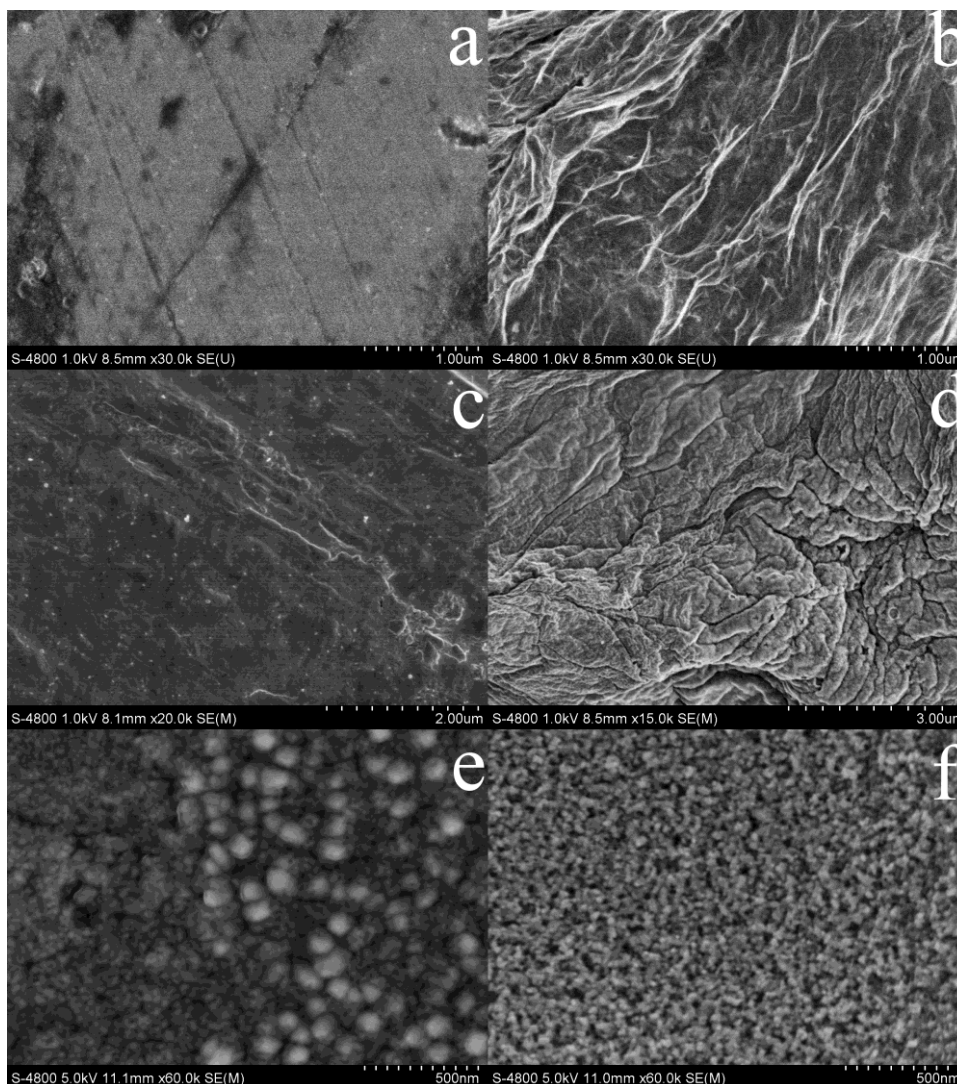


Figure 1. SEM micrographs: (a) Ti substrate, (b) Ti/rGO, and (c) Ti/RuO₂ after coating and sintering the Ru metal salt solution one time; (d) Ti/rGO-RuO₂ after coating and sintering the Ru metal salt solution one time; (e) Ti/RuO₂ after coating and sintering the Ru metal salt solution 5 times; (f) Ti/rGO-RuO₂ after coating and sintering the Ru metal salt solution 5 times.

Figures 1a and b show SEM images of the Ti substrate and Ti/rGO electrode. The surface of the Ti substrate that is not coated with graphene is flat. After electrochemical reduction of graphene oxide, the Ti substrate surface is covered with a layer of graphene (Figure 1b). After coating and sintering the Ru metal solution one time, a complete and smooth RuO₂ layer formed on the surface of the Ti substrate (Figure 1c), whereas a curled RuO₂ layer formed on Ti/rGO (Figure 1d). Finally, after coating and sintering 5 times, the surfaces of both Ti/RuO₂ and Ti/rGO-RuO₂ were completely covered with RuO₂; numerous convex RuO₂ particles appeared on the surface of Ti/RuO₂ and Ti/rGO-RuO₂, but the particles of Ti/rGO-RuO₂ were finer than those of Ti/RuO₂, and this indicates that RuO₂ crystal growth

was controlled after the addition of graphene. The specific surface area of Ti/rGO-RuO₂ is bigger than that of Ti/RuO₂, and thus, it is more conducive to water splitting.

Ti/rGO-RuO₂ and Ti/RuO₂ were analyzed using X-ray crystal diffraction to study the crystal structure of the material. As shown in Figure 2, there were two diffraction peaks at $2\theta = 27.9^\circ$ and 35.3° , and these correspond to RuO₂. The crystalline grain diameters were calculated according to the Scherrer formula using the half height width of the main diffraction peaks at $2\theta = 27.9^\circ$ and 35.3° , and the results are shown in Table 1. The crystalline grain diameters show that introducing the rGO layer into the RuO₂ coating decreased the size of the RuO₂ particles. Smaller sized crystal particles means higher catalytic activity, and thus, the catalytic activity of Ti/rGO-RuO₂ is better than that of Ti/RuO₂. Furthermore, there were diffraction peaks for Ti at $2\theta = 38.4^\circ, 40.0^\circ, 53.0^\circ, 63.0^\circ, 70.5^\circ, 76.2^\circ,$ and 77.4° because the X-ray penetrated the coating and reached the Ti substrate.

Table 1. Crystalline grain diameters of the Ti/RuO₂ and Ti/rGO-RuO₂ electrodes.

Electrode	Half height width (101 plane)	Crystallite size (101 plane)/nm
Ti/RuO ₂	0.469	18.2
Ti/rGO-RuO ₂	0.503	16.9

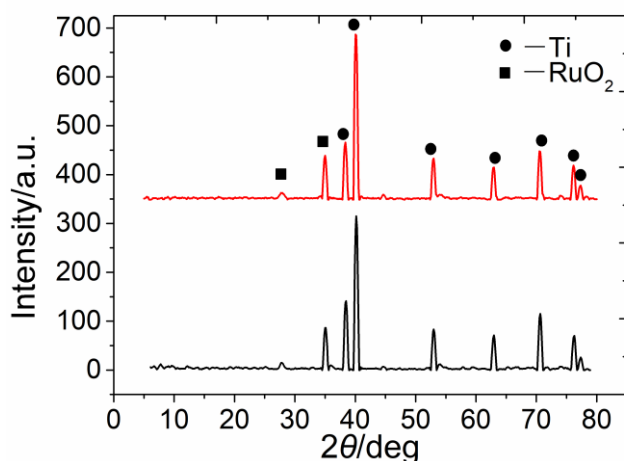


Figure 2. XRD spectra of the Ti/RuO₂ and Ti/rGO-RuO₂ electrodes.

3.2 Electrocatalytic hydrogen evolution

The electrocatalytic activity of Ti/rGO-RuO₂ for water splitting was tested in 0.1 mol·L⁻¹ NaOH using a three-electrode system. As seen in Figure 3a, the current density is too low before HER, and thus, the polarization potential at 10 mA·cm⁻² ($E_{j=10}$) was used as a reference to compare performances of the Ti/RuO₂ and Ti/rGO-RuO₂ electrodes. The hydrogen evolution potential (HEP) of the Ti/rGO-RuO₂ electrode is -1.226 V, which is lower than that of the Ti/RuO₂ electrode (-1.409 V) and that of the Pt electrode (-1.435 V). This indicates that it is easier to carry out HER on the Ti/rGO-RuO₂ electrode. At the same time, the reaction current of the Ti/rGO-RuO₂ electrode increased rapidly

over the potential range of -1.2 ~ -2.0 V, had a growth rate of 204.9 mA·V⁻¹, and had higher HER. The Ti/rGO-RuO₂ electrode has a lower Tafel slope (-93 mV·dec⁻¹) compared to the Ti/RuO₂ (-149 mV·dec⁻¹) and Pt (-134 mV·dec⁻¹) electrodes, and so this indicates that the Ti/rGO-RuO₂ electrode has excellent hydrogen evolution activity. In comparison to other reported electrodes[28-32] listed in Table 2, Ti/rGO-RuO₂ has excellent HER activity. The above results are evidence that Ti/rGO-RuO₂ has better performance for HER.

Table 2. HEP of the Ti/rGO-RuO₂ electrode and other reported DSAs.

	Electrolyte	E _{j=10} /V	
		vs.SCE	vs.RHE
Ti/rGO-RuO ₂ (this work)	0.1 mol · L ⁻¹ NaOH	-1.226	-0.213
Ti/RuO ₂ (this work)	0.1 mol · L ⁻¹ NaOH	-1.409	-0.396
Pt (this work)	0.1 mol · L ⁻¹ NaOH	-1.435	-0.422
Prorous Co phosphide/Phosphate (ref.[28])	1.0 mol · L ⁻¹ KOH	-1.393	-0.380
Ni ₂ S ₃ nanosheet array (ref.[29])	1.0 mol · L ⁻¹ NaOH	-1.236	-0.223
Co/CoO/N-doped Carbon(ref.[30])	1.0 mol · L ⁻¹ NaOH	-1.248	-0.235
CoSe/NiFe LDH(ref.[31])	1.0 mol · L ⁻¹ KOH	-1.273	-0.260
Cobalt-Embedded Nitrogen-Rich Carbon Nanotubes(ref.[32])	1.0 mol · L ⁻¹ KOH	-1.383	-0.370

There are two reasons for the excellent electrochemical activity of Ti/rGO-RuO₂. First, the higher catalytic HER activity of Ti/rGO-RuO₂ is probably due to the higher specific surface area. As seen in the SEM images shown in Figure-1, there are more and smaller convex particles on the Ti/rGO-RuO₂ coating; these enable the coating to be rougher, and this improves the number of active sites[33, 34]. Second, the rGO interlayer improves the coating conductivity. Thus, the EIS and CA curves of Ti/rGO-RuO₂ were further analyzed to prove the excellent conductivity and the number of active sites of Ti/rGO-RuO₂.

The CA curve was used to assess the electrochemically active surface area (ECSA) of the electrode. When the electrode is immersed in electrolyte, an electrochemical double-layer capacitance (EDLC) forms at the interface between the electrode and solution and is proportional to the number of exposed active sites[18, 35]. The CA curve of Ti/rGO-RuO₂ (Figure 3c) was measured at open circuit potential with a signal amplitude of 5 mV and a step time of 2 s. The EDLC and real surface area were calculated using equations (1) and (2)[36]:

$$C_d = \frac{\Delta Q}{\Delta \varphi} = \frac{\int_0^t I dt}{\Delta \varphi} \quad (1)$$

where C_d represents the electric double-layer capacitance (F), t represents the step time (s), I represents the response current (A), and $\Delta \varphi$ represents the signal amplitude (V).

$$S_r = \frac{C_d}{C_{Hg}} \quad (2)$$

where S_r represents the real surface area (cm²), C_d represents the electric double-layer capacitance (F), and $C_{Hg}=20 \mu\text{F} \cdot \text{cm}^{-2}$ represents the EDLC of pure mercury per unit area.

The EDLC results and S_r are shown in Figure 2c. The EDLC of the Ti/rGO-RuO₂ electrode is higher than that of Ti/RuO₂, which indicates that there are more exposed active sites on Ti/rGO-RuO₂.

The real surface area of the Ti/rGO-RuO₂ electrode is 475.8 cm², and this value is 1.4 times greater than that of Ti/RuO₂ (342.1 cm²); the surface roughness is also larger. Therefore, the rGO interlayer increased the active sites on the surface and improved its electrocatalytic activity of the Ti/rGO-RuO₂ electrode[37].

To further investigate the electrochemical properties of the electrodes, EIS measurements were performed at open circuit potential in 0.1 mol·L⁻¹ NaOH over the frequency range of 100 kHz to 1 Hz with an alternating signal of 5 mV. The EIS results are shown in Figure 2d. The fitting of the EIS results was described using an equivalent circuit represented by $R_s(R_f C_f)(R_{ct} C_{dl})W$, as shown in the inset of Figure 2d. In this circuit, R_s represents the solution resistance, R_f is the coating resistance, C_f is the coating capacitance, C_{dl} is the pseudo-capacitance of the double-layer, and R_{ct} is the charge transfer resistance[38, 39]. The behaviors of the circuit elements are given in Table 3, where it can be seen that the value of R_f for the Ti/rGO-RuO₂ electrode was lower than that for the Ti/RuO₂ electrode. This indicates that the rGO interlayer improved the conductivity of the coating. It is important to note that the charge transfer resistance (R_{ct}) decreased for the Ti/rGO-RuO₂ electrode, and thus, Ti/rGO-RuO₂ has higher activity for HER. In the electrocatalytic process, high conductivity can promote charge transfer and thus contribute to the high activity of Ti/rGO-RuO₂[40]. These behaviors indicate that graphene increases the electron transfer between Ti and RuO₂, thereby increasing the electrocatalytic activity of Ti/rGO-RuO₂.

Table 3. Impedance parameters of the Ti/RuO₂ and Ti/rGO-RuO₂ electrodes.

	$R_s/\Omega \cdot \text{cm}^2$	$R_f/\Omega \cdot \text{cm}^2$	$C_f/\text{F} \cdot \text{cm}^{-2}$	$R_{ct}/\Omega \cdot \text{cm}^2$	$C_{dl}/\text{F} \cdot \text{cm}^{-2}$	$W/s \cdot \text{sec}^{0.5} \cdot \text{cm}^2$	χ^2
Ti/RuO ₂	33.68	104.7	3.65×10^{-3}	5.203	9.464×10^{-5}	7.966×10^{-3}	2.63×10^{-4}
Ti/rGO-RuO ₂	30.53	98.92	3.366×10^{-3}	4.975	7.939×10^{-5}	1.311×10^{-2}	2.31×10^{-4}

The stability of the electrode is a great reference value for industrial applications. The hydrogen evolution polarization curve of Ti/rGO-RuO₂ was tested after 1000 cycles from -1.2 to 0 V at a scan rate of 100 mV·s⁻¹ in 0.1 mol·L⁻¹ NaOH solution. As seen in Figure 3e, the electrocatalytic activity of Ti/rGO-RuO₂ changed only slightly after 1000 cycles, and the polarization curve of hydrogen evolution was almost the same as the original polarization curve. The change in electrode potential at a constant current density (250 mA·cm⁻²) is shown in Figure 3f. After 1 h of electrolysis, the activities of Pt, Ti/RuO₂, and Ti/rGO-RuO₂ reached equilibrium, and the potentials were -4.617, -4.250, and -3.928 V, respectively. The potential of Ti/rGO-RuO₂ has a significant fluctuation because its excellent hydrogen evolution activity rapidly generates hydrogen, which adheres on the surface. This is particularly a problem in water splitting because gases are generated that can potentially block active sites and prohibit ionic transportation, and this is one of the major sources of overpotential. After 10 h, the surface potential of Ti/rGO-RuO₂ did not change obviously. All of the results show that Ti/rGO-RuO₂ has good stability as a hydrogen evolution catalyst. Ti/rGO-RuO₂ has high surface potential; thus, there is lower power consumption, and it is an excellent hydrogen evolution catalytic material.

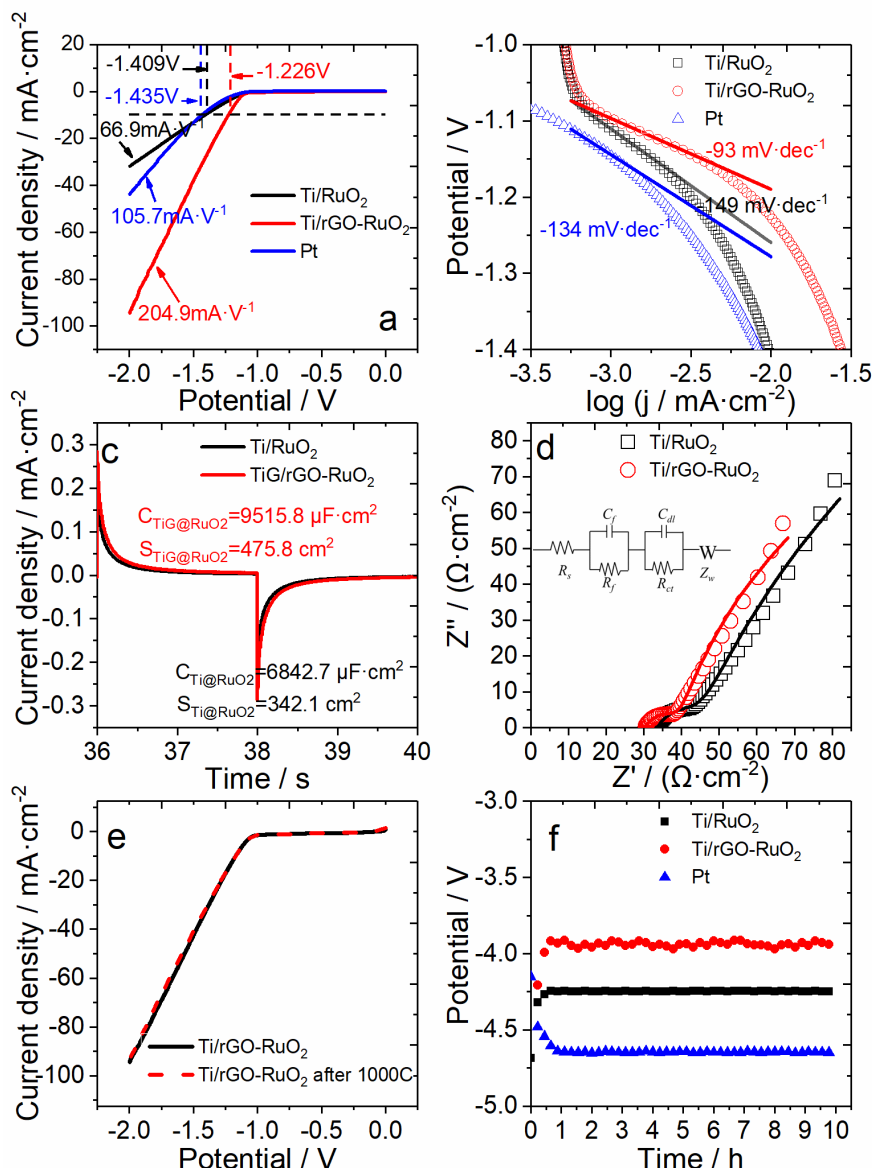


Figure 3. Electrocatalytic properties of Ti/rGO-RuO₂ for HER: (a) LSV plots obtained with Ti/RuO₂, Ti/rGO-RuO₂, and Pt for HER at 10 mV·s⁻¹ in 0.1 mol·L⁻¹ NaOH. (b) Tafel plots obtained with Ti/RuO₂, Ti/rGO-RuO₂, and Pt. (c) CA curves of Ti/RuO₂ and Ti/rGO-RuO₂ at open circuit potential with a potential step amplitude of 5 mV and pulse width of 2 s. (d) EIS spectra of Ti/RuO₂ and Ti/rGO-RuO₂ at open circuit potential over the frequency range of 0.1 Hz to 10 kHz with an alternating signal of 5 mV. (e) LSV plots of Ti/rGO-RuO₂ for HER obtained before and after 1000 cycles of cyclic voltammetry from 0 to -1.2 V (vs. SCE) with a scan rate of 100 mV·s⁻¹. (f) Chronopotentiometry of Ti/RuO₂, Ti/rGO-RuO₂, and Pt for 10 h at 250 mA·cm⁻² in 0.1 mol·L⁻¹ NaOH.

3.3 Electrocatalytic oxygen evolution

Ti/rGO-RuO₂ also has high activity for OER. Figure 4a shows the Ti/rGO-RuO₂ oxygen evolution polarization curve. The oxygen evolution potential (OEP) is 0.842 V at a current density of

$10 \text{ mA}\cdot\text{cm}^{-2}$, whereas that of Ti/RuO_2 is 0.886 V . This change can be caused by the excellent coating conductivity of $\text{Ti}/\text{rGO}-\text{RuO}_2$, as noted in the EIS analysis. The difference in OEP between $\text{Ti}/\text{rGO}-\text{RuO}_2$ and Ti/RuO_2 indicate that $\text{Ti}/\text{rGO}-\text{RuO}_2$ has obvious activity for OER. The reaction current growth rate of $\text{Ti}/\text{rGO}-\text{RuO}_2$ was $39.1 \text{ mA}\cdot\text{V}^{-1}$ at $0.8\text{-}1.0 \text{ V}$ but slows to $34.5 \text{ mA}\cdot\text{V}^{-1}$ in the range of $1.3\text{-}1.5 \text{ V}$. This is because the rate of OER for RuO_2 in alkaline solution is limited by $\text{Ru}^{4+}\text{-OH}+\text{OH}^- \rightarrow \text{Ru}^{5+}\text{-O}+\text{H}_2\text{O}+\text{e}^-$ [41]. The low concentration of OH^- in the electrolyte leads to a diffusion rate that cannot meet the requirement for OER, and thus, the current growth rate of $\text{Ti}/\text{rGO}-\text{RuO}_2$ decreases with an increase in potential.

To investigate the stability of $\text{Ti}/\text{rGO}-\text{RuO}_2$ for OER, $\text{Ti}/\text{rGO}-\text{RuO}_2$ was used as an anode for electrolysis at a constant current density of $250 \text{ mA}\cdot\text{cm}^{-2}$ until the cell voltage increased by 5 V . For comparison, Ti/RuO_2 was also tested using the same conditions. The results for this experiment are shown in Figure 4b. The continuous oxygen evolution time of $\text{Ti}/\text{rGO}-\text{RuO}_2$ is 11.4 h , whereas the oxygen evolution time of Ti/RuO_2 without a graphene layer is 9.2 h ; this indicates that the stability of $\text{Ti}/\text{rGO}-\text{RuO}_2$ for OER is better. According to a study by Chang[42], failure of electrodes is mainly caused by the formation of insulating TiO_2 . However, the rGO layer in $\text{Ti}/\text{rGO}-\text{RuO}_2$ is a conductive material with anti-oxidation ability and molecular penetration; thus, the problem of the formation of an insulating TiO_2 layer is alleviated and the service life of $\text{Ti}/\text{rGO}-\text{RuO}_2$ is prolonged.

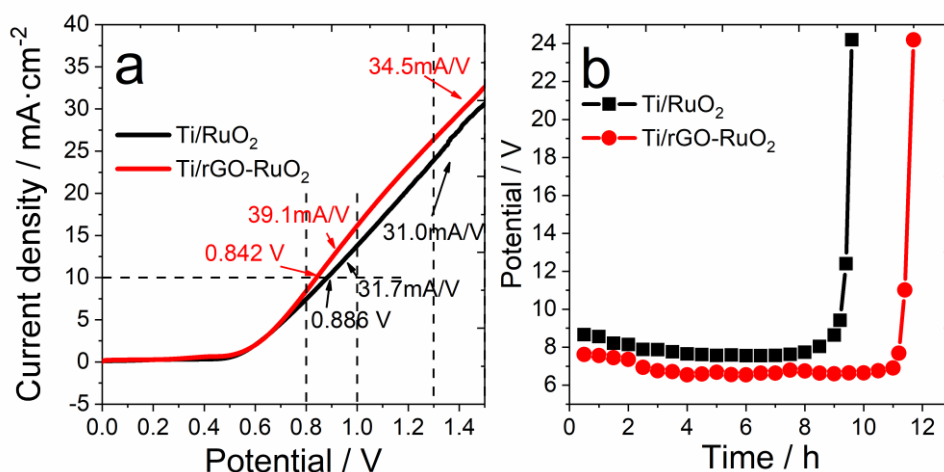


Figure 4. Electrocatalytic properties of $\text{Ti}/\text{rGO}-\text{RuO}_2$ for OER: (a) LSV plots obtained with Ti/RuO_2 and $\text{Ti}/\text{rGO}-\text{RuO}_2$ for OER at $10 \text{ mV}\cdot\text{s}^{-1}$ in $0.1 \text{ mol}\cdot\text{L}^{-1}$ NaOH and (b) chronopotentiometry of Ti/RuO_2 , $\text{Ti}/\text{rGO}-\text{RuO}_2$, and Pt for 10 h at $250 \text{ mA}\cdot\text{cm}^{-2}$ in $0.1 \text{ mol}\cdot\text{L}^{-1}$ NaOH.

$\text{Ti}/\text{rGO}-\text{RuO}_2$ electrodes were used as the anode and cathode to build a two-electrode cell to test overall water splitting. Figure 5 shows that the current density of the electrolysis cell constructed using the $\text{Ti}/\text{rGO}-\text{RuO}_2$ electrodes increased rapidly, and the current density has a linear relationship with the electrolysis cell voltage. Under the same conditions, the growth rate of the Ti/RuO_2 current density decreases with an increase in cell voltage, and this indicates that the reaction rate on Ti/RuO_2 reaches a limit. The electrolytic cell constructed using the $\text{Ti}/\text{rGO}-\text{RuO}_2$ electrodes demonstrated excellent catalytic activity and delivered a current density of $34.3 \text{ mA}\cdot\text{cm}^{-2}$ with an applied voltage of 3.0 V . This current density is higher than that of $\text{Ti}/\text{rGO}-\text{RuO}_2$ ($23.0 \text{ mA}\cdot\text{cm}^{-2}$), and therefore, $\text{Ti}/\text{rGO}-\text{RuO}_2$ can lower energy consumption for the water electrode reaction.

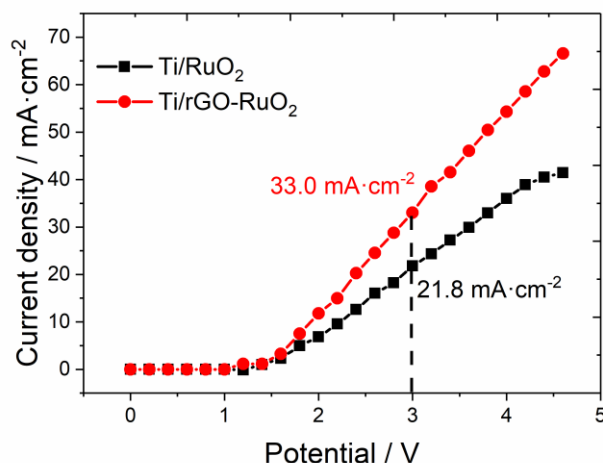


Figure 5. Current density of an electrolytic cell using Ti/rGO-RuO₂ electrodes as the anode and cathode at different cell voltages in 0.1 mol·L⁻¹ NaOH.

4. CONCLUSIONS

In summary, this paper presents the Ti/rGO-RuO₂ electrode for overall water splitting. The Ti/rGO-RuO₂ electrode is prepared using a method in which the Ti substrate is covered with electrochemically reduced GO then coated with RuO₂ via thermal decomposition. This method can be easily industrialized. The prepared Ti/rGO-RuO₂ electrode has many excellent properties such as high catalytic activity; it also has high stability for electrochemical reactions (OER and HER). According to SEM images, adding an rGO layer as an intermediate layer leads to the formation of finer RuO₂ particles on the surface of the Ti/rGO-RuO₂ electrode, and this provides more active sites as catalytic centers. The CA curve shows that the real surface area of the Ti/rGO-RuO₂ electrode is larger than that of Ti/RuO₂; specifically, it is 1.4 times larger than that of Ti/RuO₂. At an applied current density of 10 mA·cm⁻², Ti/rGO-RuO₂ has a lower HEP of -1.226 V and OEP of 0.842 V compared to Ti/RuO₂. In addition, the EIS of Ti/rGO-RuO₂ indicates that the graphene layer decreases the coating resistance (R_f) and the coating transfer resistance (R_{ct}), and this enables the current to react more efficiently through the metal sites. Therefore, Ti/rGO-RuO₂ has obviously high catalytic activity.

ACKNOWLEDGMENT

The authors gratefully acknowledge the financial support of the Zhejiang Province Nature Science Foundation of China under grant number LY18E040002.

References

1. S. Siracusano, V. Baglio, A.D. Blasi, N. Briguglio, A. Stassi, R. Ornelas, E. Trifoni, V. Antonucci, A.S. Aricò, *International Journal of Hydrogen Energy*, 35 (2010) 5558.
2. A.A. Gewirth, M.S. Thorum, *Cheminform*, 49 (2010) 3557.
3. F.D. Kong, S. Zhang, G.P. Yin, Z.B. Wang, C.Y. Du, G.Y. Chen, N. Zhang, *International Journal of*

- Hydrogen Energy*, 37 (2012) 59.
4. K.S. Exner, J. Anton, T. Jacob, H. Over, *Angewandte Chemie*, 55 (2016) 7501.
 5. H.O. Prof, M. Knapp, E. Lundgren, A.P. Seitsonen, M. Schmid, P. Varga, *Chemphyschem*, 5 (2004) 167.
 6. H. Over, A.P. Seitsonen, E. Lundgren, M. Wiklund, J.N. Andersen, *Chemical Physics Letters*, 342 (2001) 467.
 7. K. Reuter, M. Scheffler, *Physical Review B Condensed Matter*, 65 (2001) 321.
 8. Q. Sun, K. Reuter, M. Scheffler, *Phys.rev.b*, 67 (2003) 920.
 9. L. Giordano, B. Han, M. Risch, W.T. Hong, R.R. Rao, K.A. Stoerzinger, S.H. Yang, *Catalysis Today*, 262 (2016) 2.
 10. S. Cherevko, S. Geiger, O. Kasian, N. Kulyk, J.P. Grote, A. Savan, B.R. Shrestha, S. Merzlikin, B. Breitbach, A. Ludwig, *Catalysis Today*, 262 (2016) 170.
 11. Z. Wu, Y. Duan, S. Ge, A.C.K. Yip, F. Yang, Y. Li, T. Dou, *Catalysis Communications*, 91 (2017) 10.
 12. A. Li, Y. Hu, M. Yu, X. Liu, M. Li, *International Journal of Hydrogen Energy*, 42 (2017) 9419.
 13. L. Qi, Y. Li, L. Liu, J. Zhou, Y. Ai, Z. Tang, J. Wang, H. Bao, C. Zhang, Q. Liang, *Chemistryselect*, 2 (2017) 8288.
 14. W. Ye, Y. Ge, Z. Gao, R. Lu, S. Zhang, *Sustainable Energy & Fuels*, 1 (2017) 2128.
 15. M.D. Stoller, S. Park, Y. Zhu, J. An, R.S. Ruoff, *Nano Letters*, 8 (2008) 3498.
 16. K.S. Novoselov, A.K. Geim, S.V. Morozov, D. Jiang, M.I. Katsnelson, I.V. Grigorieva, S.V. Dubonos, A.A. Firsov, *Nature*, 438 (2005) 197.
 17. A. Fasolino, J.H. Los, M.I. Katsnelson, *Nature Materials*, 6 (2007) 858.
 18. A.A. Balandin, S. Ghosh, W. Bao, I. Calizo, D. Teweldebrhan, F. Miao, C.N. Lau, *Eprint Arxiv*, 8 (2008) 902.
 19. K.R. Yoon, G.Y. Lee, J.W. Jung, N.H. Kim, S.O. Kim, I.D. Kim, *Nano Letters*, 16 (2016) 2076.
 20. M. Wu, Y.J. Ju, S.J. Kim, Y. Kang, H.T. Jung, H.K. Jung, *Rsc Advances*, 6 (2016) 23467.
 21. X. Zeng, D. Dang, L. Leng, C. You, G. Wang, C. Zhu, S. Liao, *Electrochimica Acta*, 192 (2016) 431.
 22. V.D. Dao, L.L. Larina, J.K. Lee, K.D. Jung, B.T. Huy, H.S. Choi, *Carbon*, 81 (2015) 710.
 23. Y.J. Yang, X. Hu, Z. Xu, *Fullerenes Nanotubes & Carbon Nanostructures*, 25 (2017) 435.
 24. T. Bhowmik, M.K. Kundu, S. Barman, *Acs Applied Materials & Interfaces*, 8 (2016) 28678.
 25. O.C. Compton, S. Kim, C. Pierre, J.M. Torkelson, S.T. Nguyen, *Advanced Materials*, 22 (2010) 4759.
 26. J.S. Qi, J.Y. Huang, J. Feng, D.N. Shi, J. Li, *Acs Nano*, 5 (2011) 3475.
 27. S. Chen, L. Brown, M. Levendorf, W. Cai, S.Y. Ju, J. Edgeworth, X. Li, C.W. Magnuson, A. Velamakanni, R.D. Piner, *Acs Nano*, 5 (2010) 1321.
 28. Y. Yang, H. Fei, G. Ruan, J.M. Tour, *Advanced Materials*, 27 (2015) 3175.
 29. L.L. Feng, G. Yu, Y. Wu, G.D. Li, H. Li, Y. Sun, T. Asefa, W. Chen, X. Zou, *Journal of the American Chemical Society*, 137 (2015) 14023.
 30. H. Jin, J. Wang, D. Su, Z. Wei, Z. Pang, Y. Wang, *Journal of the American Chemical Society*, 137 (2015) 2688.
 31. Y. Hou, M.R. Lohe, J. Zhang, S. Liu, X. Zhuang, X. Feng, *Energy & Environmental Science*, 9 (2015) 478.
 32. X. Zou, X. Huang, A. Goswami, R. Silva, B.R. Sathe, E. Mikmeková, T. Asefa, *Angewandte Chemie*, 126 (2014) 4461.
 33. H. Liu, P. He, Z. Li, J. Li, *Nanotechnology*, 17 (2006) 2167.
 34. H. Liu, Y. Liu, J. Li, *Physical Chemistry Chemical Physics Pccp*, 12 (2010) 1685.
 35. M. Jiang, H. Wang, Y. Li, H. Zhang, G. Zhang, Z. Lu, X. Sun, L. Jiang, *Small*, 13 (2017) 1602240.
 36. C.S. Dai, B. Zhang, D.L. Wang, T.F. Yi, X.G. Hu, *Journal of Alloys & Compounds*, 422 (2006) 332.
 37. G. Ye, Y. Gong, J. Lin, B. Li, Y. He, S.T. Pantelides, W. Zhou, R. Vajtai, P.M. Ajayan, *Nano Letters*,

- 16 (2016) 1097.
38. S.M. Hoseinieh, F. Ashrafizadeh, *Ionics*, 19 (2013) 113.
39. S.M. Hoseinieh, F. Ashrafizadeh, M.H. Maddahi, *Journal of the Electrochemical Society*, 157 (2010) E50.
40. J. Duan, S. Chen, C. Zhao, *Nature Communications*, 8 (2017) 15341.
41. R.R. Rao, M.J. Kolb, N.B. Halck, A.F. Pedersen, A. Mehta, H. You, K.A. Stoerzinger, Z. Feng, H.A. Hansen, H. Zhou, *Energy & Environmental Science*, 10 (2017) 2626.
42. L. Chang, Y. Zhou, X. Duan, W. Liu, D. Xu, *Journal of the Taiwan Institute of Chemical Engineers*, 45 (2014) 1338.

© 2018 The Authors. Published by ESG (www.electrochemsci.org). This article is an open access article distributed under the terms and conditions of the Creative Commons Attribution license (<http://creativecommons.org/licenses/by/4.0/>).